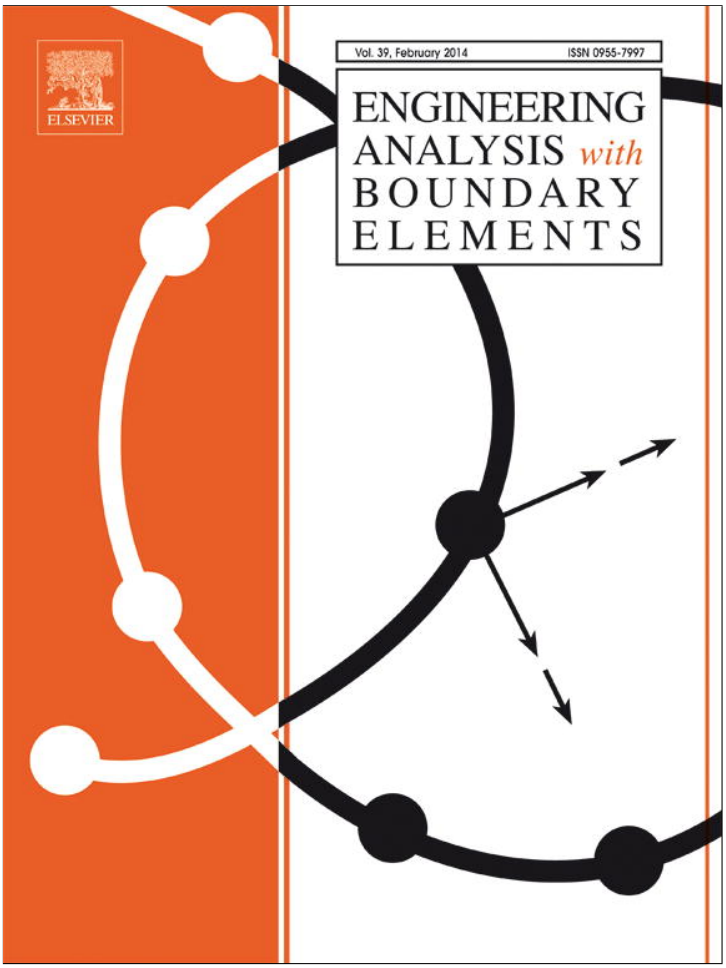

Engineering Analysis with Boundary Elements 39 (2014) 44–52

Contents lists available at ScienceDirect

Engineering Analysis with Boundary Elements

journal homepage: www.elsevier.com/locate/enganabound

Velocity–vorticity RANS turbulence modeling by boundary element method

Janez Lupše, Leopold Škerget, Jure Ravnik*

Faculty of Mechanical Engineering, University of Maribor, Smetanova 17, SI-2000 Maribor, Slovenia

ARTICLE INFO

Article history:
Received 23 October 2012
Accepted 1 November 2013
Available online 21 November 2013

Keywords:
Boundary element method
Velocity–vorticity
Turbulence model
RANS

ABSTRACT

Turbulent flow over various geometries is studied numerically. Incompressible set of Navier–Stokes equations is considered and solved by boundary domain integral method (BDIM). Governing equations are written in velocity–vorticity form. Turbulence models used are based on eddy-viscosity hypothesis. Integral form of equations, discretization and the solution algorithm are presented. The algorithm is tested with two separate test cases. The first is the turbulent channel flow for two different Reynolds numbers: $Re_\tau = 180$ and $Re_\tau = 395$. Results show very good agreement with corresponding DNS data. The second test case is the flow over backward facing step for Reynolds number $Re_h = 5000$, which shows good agreement with literature data on mean reattachment length.

1. Introduction

Ever since the early 70s of the last century, boundary element method (BEM) has been seen as a very successful method for discretization of governing equations for numerous problems. Its advantage is the use of Green's functions as weighting functions, which allows the method to capture some or all of the physics of the governing phenomena. If the physics of the problem is properly captured by the fundamental solution, then only the boundary of the domain needs to be discretized and thus discretization of the interior of the problem domain is avoided. Although great success was achieved with boundary elements in many areas, discretization of Navier–Stokes equations by BEM is more challenging since they are of strongly nonlinear parabolic convective–diffusive type. Fundamental solutions which would solve those types of equations are not known, thus we are limited to the usage of fundamental solutions describing only the linear part of problem's physics. The advantage of discretization of only boundary is thus lost. This and the complexity of the method lead to neglection of BEM usage for fluid flow problems. Even though discretization of whole solution domain is needed, the existence of Green's functions that can capture dominant physics in fluid flow makes usage of BEM appealing for this kind of problems.

Many authors developed different approaches in order to cope with domain discretization. Among others, DR(dual reciprocity)-BEM was developed by Wrobel et al. [1] for transient heat conduction. It was later expanded to nonlinear diffusion problems by Wrobel and Brebbia [2] and convection–diffusion problems by Wrobel and DeFigueiredo [3]. Furthermore, the so-called GEM (Green element method) was developed by Taigbenu [4] which involves cell integration. Popov and Power [5] described the MD-DRM (multi-domain dual reciprocity method) for solving domain dominant problems, which was then applied to Navier–Stokes system [6] and solved quite successfully thermal convection problems as seen in Florez et al. [7].

In the 80s of the previous century BEM was successfully applied to velocity–vorticity form of Navier–Stokes equations by Škerget and Alujeviè [8]. Since then, the method was applied to a wide range of fluid flow problems. The method shows great promise in solving laminar isothermal and non-isothermal [9,10] flows. However, while vorticity transport equation is rather simple for two-dimensional flows with constant material properties, its complexity (and nonlinearity) increases greatly when used in three-dimensional flows or when derived from Reynolds averaged (RANS) equations. Thus, solutions for turbulent flows with RANS equations proved to be much more difficult than solving vorticity transport equation in its original form. Recently, a few other attempts were made to solve turbulent fluid flow with boundary element method. An attempt made by Ramšak and Škerget [11] used stream function-vorticity equation which solved turbulent flows in two-dimensions quite successfully, but was hindered by problems of extrapolating this approach in three-dimensions. Furthermore, a few attempts were made by different combinations of other discretization methods with BEM, such as Ravnik et al. [12].

In this paper we present application of BEM-based algorithm to turbulent fluid flows described by Reynolds averaged vorticity transport equation. Solution of kinematics equation, which provides

* Corresponding author.
E-mail address: jure.ravnik@um.si (J. Ravnik).

0955-7997/$ - see front matter © 2013 Elsevier Ltd. All rights reserved.
http://dx.doi.org/10.1016/j.enganabound.2013.11.004

values of vorticity on the domain boundary, is solved by standard single domain BEM. All other transport equations are then solved by subdomain BEM as described in Ramšak and Škerget [13]. Although the algorithm is written for planar flows, the advantage of the velocity–vorticity formulation over the stream-function-vorticity formulation is the fact that the governing equations can be extended into three dimensions. Turbulence models based on eddy-viscosity hypothesis are considered. Also, a variety of fundamental solutions is used in order to reflect governing physics as close to reality as possible. Two different cases of turbulent flows are considered in order to test the implementation of developed algorithm. Steady flow in a channel is the first test case presented, followed by flow over a backward facing step.

2. Governing equations

2.1. Primitive variables formulation

The governing equations for incompressible viscous flow are the Navier–Stokes equations. Written for primitive variables in Reynolds averaged form, they are composed of continuity and momentum equations, if we disregard non-isothermal flows. These are:

$$\frac{\partial U_i}{\partial x_i}=0, \tag{1}$$

$$\rho\frac{\partial U_i}{\partial t}+\rho U_j\frac{\partial U_i}{\partial x_j}=-\frac{\partial P}{\partial x_i}+\frac{\partial}{\partial x_j}\left(\eta_0\frac{\partial U_i}{\partial x_j}-\rho\overline{u_iu_j}\right)+\rho g_i, \tag{2}$$

where U_i represents i-th component of averaged velocity vector, P the averaged pressure field, η_0 the dynamic viscosity, ρ the mass density and g_i the i-th component of the gravity acceleration vector. u_i represents fluctuating part of velocity.

Since in these equations additional unknowns are present in the form of Reynolds stresses ($\overline{u_iu_j}$), some kind of closure model needs to be included. Employing an eddy-viscosity model, Reynolds stress tensor can be modeled via Boussinesq hypothesis (written for incompressible flow):

$$\overline{u_iu_j}=-\nu_t\left(\frac{\partial U_i}{\partial x_j}+\frac{\partial U_j}{\partial x_i}\right). \tag{3}$$

ν_t represents turbulent viscosity which is calculated using a turbulence model.

2.2. Velocity–vorticity formulation

In order to derive the RANS form of the vorticity transport equation (see Škerget and Ravnik [10]), Eq. (2) should be rewritten as

$$\frac{\partial U_i}{\partial t}+U_j\frac{\partial U_i}{\partial x_j}=-e_{ijk}\frac{\partial \nu_{eff}\omega_k}{\partial x_j}+2e_{ijk}\frac{\partial \nu_{eff}}{\partial x_j}\omega_k+2\frac{\partial \nu_{eff}}{\partial x_j}\frac{\partial U_i}{\partial x_j}-\frac{\partial P}{\partial x_i}+\frac{\rho}{\rho_0}g_i, \tag{4}$$

where ω_k represents k-th component of averaged vorticity field and ν_{eff} total or effective kinematic viscosity, composed of molecular and additional modeled kinematic viscosity ($\nu_{eff}=\nu_0+\nu_t$). Boussinesq approximation of density was used in buoyancy term while for other terms constant density (ρ_0) is used.

By applying curl differential operator to Eq. (4) the averaged form of vorticity equation is then obtained. For two-dimensional form of averaged flows averaged vorticity transport equation can then be written as

$$\frac{\partial \omega}{\partial t}+U_j\frac{\partial \omega}{\partial x_j}=\nu_0\frac{\partial^2\omega}{\partial x_j\partial x_j}-\frac{1}{\rho_0}e_{ij}\frac{\partial \rho g_i}{\partial x_j}-\frac{1}{\rho_0}e_{ij}\frac{\partial f_i^m}{\partial x_j}, \tag{5}$$

where f_i^m is

$$f_i^m=-e_{ij}\frac{\partial \nu_t\omega}{\partial x_j}+2e_{ij}\frac{\partial \nu_t}{\partial x_j}\omega+2\frac{\partial \nu_t}{\partial x_j}\frac{\partial U_i}{\partial x_j} \tag{6}$$

and is treated as a nonlinear source term.

Since boundary conditions for vorticity are a priory unknown, an additional equation is needed. It can be derived with help of vorticity definition and continuity equation [9]. The derived equation is of simple elliptic type and represents kinematic constraints between vorticity and velocity fields:

$$\frac{\partial^2 U_i}{\partial x_j\partial x_j}+e_{ij}\frac{\partial \omega}{\partial x_k}=0. \tag{7}$$

As mentioned before, RANS equations need to be closed by a turbulence model. The goal is to reproduce additional turbulent viscosity (ν_t) in such a way to recover flow field as close to reality as possible. For this purpose we have used 1-equation Spalart–Allmaras [14] turbulence model and some variations of 2-equation k–ε type models, namely Chien [15] turbulence model and Abe–Kondoh–Nagano [16] turbulence model. A generic transport equation for these types of models can be written as

$$\frac{\partial \phi}{\partial t}+U_j\frac{\partial \phi}{\partial x_j}=\frac{\partial}{\partial x_j}\left[\nu_{eff}\frac{\partial \phi}{\partial x_j}\right]+P-D, \tag{8}$$

where ϕ is transport variable which represents turbulent kinetic energy (k), its dissipation (ε) or modified turbulent viscosity ($\tilde{\nu}$), depending on the model and equation used. In Eq. (8) P and D stand for production and destruction terms and are defined in Table 1. Again, ν_{eff} stands for total or effective kinematic viscosity.

Destruction terms in turbulence models usually include higher order dependence of transported variable in a given equation which is why linearization of those terms is advisable for stabilization of solution of Eq. (8). This can be done by splitting quadratic dependence of term to

$$D=\mathrm{Arg}\cdot(\phi^2)\Rightarrow \mathrm{Arg}\cdot(\phi_{(it)})(\phi_{(it-1)}), \tag{9}$$

where Arg represents the argument of destruction term, dependent on the model used, and index (it) represents current and ($it-1$) previous iteration value.

3. Integral equations

Since BEM is an integral method, governing equations need to be recast in an integral form prior to discretization. The basis of BEM can be found in Wrobel and Aliabadi [17] for example while integral equations and their derivation for flow kinematics and vorticity kinetics can be found in Škerget and Ravnik [10]. Let us denote problem domain by Ω and its boundary by Γ. The basic

Table 1
Turbulence models used. SA stands for the Spalart–Allmaras, CH for the Chiens and ABE for the Abe–Kondoh–Nagano turbulence models.

Model	ϕ	Wall b.c.	P	D
SA [14]	$\tilde{\nu}$	$(\tilde{\nu})_w=0$	$P=c_{b1}[1-f_{t2}]\tilde{S}\tilde{\nu}+\frac{1}{\sigma}c_{b2}\left(\frac{\partial\tilde{\nu}}{\partial x_j}\right)^2$	$D=\left[c_{w1}f_w-\frac{c_{b1}}{\kappa^2}\right]\left[\frac{\tilde{\nu}}{d_n}\right]^2$
CH [15]	k	$(k)_w=0$	$P_k=\nu_t\left(\frac{\partial U_i}{\partial x_j}+\frac{\partial U_j}{\partial x_i}\right)\frac{\partial U_i}{\partial x_i}$	$D_k=2\nu\frac{k}{d_n^2}+\varepsilon$
CH [15]	ε	$(\varepsilon)_w=0$	$P_\varepsilon=c_{\varepsilon1}f_1P_k\frac{\varepsilon}{k}$	$D_\varepsilon=c_{\varepsilon2}f_2\frac{\varepsilon^2}{k}$
ABE [16]	k	$(k)_w=0$	$P_k=\nu_t\left(\frac{\partial U_i}{\partial x_j}+\frac{\partial U_j}{\partial x_i}\right)\frac{\partial U_i}{\partial x_i}$	$D_k=\varepsilon$
ABE [16]	ε	$(\varepsilon)_w=\nu_0\frac{\partial^2k}{\partial d_n^2}$	$P_\varepsilon=c_{\varepsilon1}P_k\frac{\varepsilon}{k}$	$D_\varepsilon=c_{\varepsilon2}f_\varepsilon\frac{\varepsilon^2}{k}$

form of kinematics equation (7) can now be written in an integral form for solution domain as

$$c(\xi)U_i(\xi)+\int_\Gamma U_i\frac{\partial u^*}{\partial n}\,d\Gamma-\int_\Gamma\frac{\partial U_i}{\partial n}u^*\,d\Gamma = e_{ij}\int_\Gamma \omega n_j u^*\,d\Gamma - e_{ij}\int_\Omega \omega\frac{\partial u^*}{\partial x_j}\,d\Omega, \tag{10}$$

where u^* represents the Laplace fundamental solution:

$$u^*=\frac{1}{2\pi}\ln\frac{1}{r} \tag{11}$$

and r represents the distance between source and reference point.

Another equation derived from Eq. (7) is needed in order to obtain the equation for unknown boundary vorticity values (see Škerget and Ravnik [10]):

$$c(\xi)U_i(\xi)+\int_\Gamma U_i\frac{\partial u^*}{\partial n}\,d\Gamma = e_{ij}\int_\Gamma U_j\frac{\partial u^*}{\partial t}\,d\Gamma - e_{ij}\int_\Omega \omega\frac{\partial u^*}{\partial x_j}\,d\Omega, \tag{12}$$

where n represents unit normal and t unit tangent.

Integral form of the vorticity transport equation (5) is

$$\begin{aligned}\int_\Omega\frac{\partial\omega}{\partial t}u^*\,d\Omega+\int_\Gamma\omega U_j n_j u^*\,d\Gamma-\int_\Omega\omega U_j\frac{\partial u^*}{\partial x_j}\,d\Omega &= \nu_0\left[-c(\xi)\omega(\xi)-\int_\Gamma\omega\frac{\partial u^*}{\partial n}\,d\Gamma+\int_\Gamma\frac{\partial\omega}{\partial n}u^*\,d\Gamma\right]\\ &-e_{ij}\frac{1}{\rho_0}\left[\int_\Gamma\rho g_i n_j u^*\,d\Gamma+\int_\Omega\rho g_i\frac{\partial u^*}{\partial x_j}\right]\\ &-e_{ij}\left[\int_\Gamma f_i^m n_j u^*\,d\Gamma+\int_\Omega f_i^m\frac{\partial u^*}{\partial x_j}\,d\Omega\right].\end{aligned} \tag{13}$$

The vorticity convection term was transformed by the Gauss theorem while the diffusion mechanism is described by the Green function used.

In order to derive an integral equation for Eq. (8) effective viscosity needs to be split to constant and variable parts ($\nu_{eff}=\nu_0+\nu_t$) and the equation multiplied by Green function as a weighting function:

$$\nu_0\frac{\partial^2\phi}{\partial x_j\partial x_j}u^*=\frac{D\phi}{Dt}u^*-\frac{\partial}{\partial x_j}\left[\nu_t\frac{\partial\phi}{\partial x_j}\right]u^*-(P-D)u^*. \tag{14}$$

With the use of Laplace fundamental solution (11) the following boundary-domain integral statement can be derived:

$$\nu_0\left(c(\xi)\phi(\xi)+\int_\Gamma\phi\frac{\partial u^*}{\partial n}\,d\Gamma-\int_\Gamma\frac{\partial\phi}{\partial n}u^*\,d\Gamma\right) = -\int_\Omega\frac{D\phi}{Dt}u^*\,d\Omega+\int_\Omega\frac{\partial}{\partial x_j}\left[\nu_t\frac{\partial\phi}{\partial x_j}\right]u^*\,d\Omega+\int_\Omega(P-D)u^*\,d\Omega. \tag{15}$$

Since nonlinear diffusion term on the right-hand side of Eq. (15) includes higher order derivatives of variable in question, it should be written differently. One possibility to reduce the order of the function derivative is to write

$$\int_\Omega\frac{\partial}{\partial x_j}\left[\nu_t\frac{\partial\phi}{\partial x_j}\right]u^*\,d\Omega=\int_\Omega\frac{\partial}{\partial x_j}\left(\nu_t\frac{\partial\phi}{\partial x_j}u^*\right)d\Omega-\int_\Omega\nu_t\frac{\partial\phi}{\partial x_j}\frac{\partial u^*}{\partial x_j}\,d\Omega. \tag{16}$$

First term on the right-hand side is now transformed with help of Gauss's theorem to

$$\int_\Omega\frac{\partial}{\partial x}\left(\nu_t\frac{\partial\phi}{\partial x_j}u^*\right)d\Omega=\int_\Gamma\nu_t n_j\frac{\partial\phi}{\partial x_j}u^*\,d\Gamma. \tag{17}$$

Similarly, the derivative from the convective part is removed. First let us write an expanded form of the convective term:

$$\int_\Omega\frac{D\phi}{Dt}u^*\,d\Omega=\int_\Omega\frac{\partial\phi}{\partial t}u^*\,d\Omega+\int_\Omega U_j\frac{\partial\phi}{\partial x_j}u^*\,d\Omega. \tag{18}$$

For the use with Laplace fundamental solution, Eq. (18) can be recast as

$$\int_\Omega\frac{D\phi}{Dt}u^*\,d\Omega=\int_\Omega\frac{\partial\phi}{\partial t}u^*\,d\Omega+\int_\Gamma U_j\phi n_j u^*\,d\Gamma-\int_\Omega U_j\phi\frac{\partial u^*}{\partial x_j}\,d\Omega. \tag{19}$$

For elliptic fundamental solutions the local time derivative also needs to be considered. Finite difference approximation on time axis is applied. In first two time steps, the non-symmetric first order two-time level Euler implicit scheme is used, see Eq. (20a). In all the subsequent time steps, the second order asymmetric differences scheme is used, as can be seen in Eq. (20b):

$$\int_\Omega\frac{\partial\phi}{\partial t}u^*\,d\Omega\approx\int_\Omega\frac{\phi_F-\phi_{F-1}}{\Delta t}u^*\,d\Omega, \tag{20a}$$

$$\int_\Omega\frac{\partial\phi}{\partial t}u^*\,d\Omega\approx\int_\Omega\frac{3\phi_F-4\phi_{F-1}+\phi_{F-2}}{2\Delta t}u^*\,d\Omega. \tag{20b}$$

Δt represents time step and indices F, $F-1$ and $F-2$ represent current, previous and pre-previous time step values. In subsequent equations index F denoting current time step is omitted. Also constants α, β, γ with values $\alpha=1/\Delta t$, $\beta=-1/\Delta t$ and $\gamma=0$ are used for non-symmetric first order two-time level Euler implicit scheme and $\alpha=3/(2\Delta t)$, $\beta=-2/(\Delta t)$ and $\gamma=1/(2\Delta t)$ are used for second order asymmetric differences scheme. The final form of integral representation of Eq. (8) with the use of Laplace fundamental solution is then

$$\begin{aligned}c(\xi)\phi(\xi,t_F)+\int_\Gamma\phi\frac{\partial u^*}{\partial n}\,d\Gamma-\int_\Gamma\frac{\partial\phi}{\partial n}u^*\,d\Gamma &= -\frac{1}{\nu_0}\int_\Omega(\alpha\phi+\beta\phi_{F-1}+\gamma\phi_{F-2})u^*\,d\Omega\\ &-\frac{1}{\nu_0}\left(\int_\Gamma U_j\phi n_j u^*\,d\Gamma-\int_\Omega U_j\phi\frac{\partial u^*}{\partial x_j}\,d\Omega\right)\\ &+\frac{1}{\nu_0}\left(\int_\Gamma\nu_t n_j\frac{\partial\phi}{\partial x_j}u^*\,d\Gamma-\int_\Omega\nu_t\frac{\partial\phi}{\partial x_j}\frac{\partial u^*}{\partial x_j}\,d\Omega\right)\\ &+\frac{1}{\nu_0}\int_\Omega(P-D)u^*\,d\Omega.\end{aligned} \tag{21}$$

Eq. (8) is of convective–diffusive type, thus linear convection–diffusion fundamental solution can also be used instead of Laplace fundamental solution. In order to apply this type of fundamental solution velocity field needs to be split into homogeneous and variable parts ($U_j=\overline{u_j}+u_j'$). Homogeneous part of convection can then be included into fundamental solution itself as $Q^*=\partial u^*/\partial n+(\overline{u_j}n_j/\nu_0)u^*$. This gives us the following equation:

$$\begin{aligned}c(\xi)\phi(\xi,t_F)+\int_\Gamma\phi Q^*\,d\Gamma-\int_\Gamma\frac{\partial\phi}{\partial n}u^*\,d\Gamma &= -\frac{1}{\nu_0}\int_\Omega(\beta\phi_{F-1}+\gamma\phi_{F-2})u^*\,d\Omega\\ &-\frac{1}{\nu_0}\left(\int_\Gamma(U_j-\overline{u_j})\phi n_j u^*\,d\Gamma-\int_\Omega(U_j-\overline{u_j})\phi\frac{\partial u^*}{\partial x_j}\,d\Omega\right)\\ &+\frac{1}{\nu_0}\left(\int_\Gamma\nu_t n_j\frac{\partial\phi}{\partial x_j}u^*\,d\Gamma-\int_\Omega\nu_t\frac{\partial\phi}{\partial x_j}\frac{\partial u^*}{\partial x_j}\,d\Omega\right)\\ &+\frac{1}{\nu_0}\int_\Omega(P-D)u^*\,d\Omega,\end{aligned} \tag{22}$$

where u^* is now convection–diffusion fundamental solution:

$$u^*=\frac{1}{2\pi\nu_0}K_0(\mu r)e^{\overline{u_j}r_j/2\nu_0},\quad \mu^2=\left(\frac{\overline{u_j}}{2\nu_0}\right)^2+\frac{\alpha}{2\nu_0}, \tag{23}$$

where K_0 is a modified Bessel function of the second kind of order 0.

Finally, it is also possible to use parabolic diffusion fundamental solution instead of Laplace for time dependent problems. In that case, finite difference approximation of local time derivative is not needed and additional term for initial conditions

$((1/\nu_0)\int_\Omega \phi_{F-1} u^*_{F-1}\, d\Omega)$ is present on the right-hand side of the equation (see Škerget and Samec [18] for derivation of vorticity transport equation with parabolic diffusion fundamental solution).

4. Discrete form

For calculation of boundary vorticity values by Eq. (12) the single domain BEM is used. For all other equations the subdomain method is preferred, since both memory and CPU time savings can be substantial with it. Domain and boundary integrals obtained from Eq. (21) or (22) are then approximated as $\Gamma \approx \sum_{e=1}^{E} \Gamma_e$ and $\Omega \approx \sum_{c=1}^{C} \Omega_c$. Over each subdomain and corresponding boundary elements, function and normal derivative values need to be interpolated. In our case quadratic ($\phi \approx \{\Phi\}^T[\phi]^n$) and biquadratic ($\phi \approx \{\psi\}^T[\phi]^n$) interpolation was used for boundary and domain function values while constant interpolation ($\phi \approx \{\chi\}^T[\phi]^n$) was used for normal derivatives. This gives us a nine-node Lagrangian cell as shape of each subdomain. Using described approximations we can write the following discretized equation for Eq. (21):

$$\begin{aligned}
&\frac{1}{\nu_0}\sum_{c=1}^{C}\{b\}^T\{\alpha\phi+\beta\phi_{F-1}+\gamma\phi_{F-2}\}^n \\
&\quad+\frac{1}{\nu_0}\sum_{e=1}^{E}\{a_j\}^T\{U_j\phi\}^n-\frac{1}{\nu_0}\sum_{c=1}^{C}\{d_j\}^T\{U_j\phi\}^n \\
&\quad=-\left(c(\xi)\phi(\xi,t_F)+\sum_{e=1}^{E}\{h\}^T\{\phi\}^n-\sum_{e=1}^{E}\{g\}^T\left\{\frac{\partial\phi}{\partial n}\right\}^n\right) \\
&\qquad+\frac{1}{\nu_0}\sum_{e=1}^{E}\{a_j\}^T\left\{\nu_t\frac{\partial\phi}{\partial x_j}\right\}^n-\frac{1}{\nu_0}\sum_{c=1}^{C}\{d_j\}^T\left\{\nu_t\frac{\partial\phi}{\partial x_j}\right\}^n \\
&\qquad+\frac{1}{\nu_0}\sum_{c=1}^{C}\{b\}^T\{(P-D)\}^n,
\end{aligned} \tag{24}$$

where we have denoted integrals of interpolation functions and the fundamental solution by

$$\begin{aligned}
&h^n_e=\int_{\Gamma_e}\Phi^n\frac{\partial u^*}{\partial n}\,d\Gamma,\quad g^n_e=\int_{\Gamma_e}\chi^n u^*\,d\Gamma,\\
&a^n_{e,j}=\int_{\Gamma_e}\Phi^n n_j u^*\,d\Gamma,\quad d^n_{c,j}=\int_{\Omega_c}\psi^n\frac{\partial u^*}{\partial x_j}\,d\Omega,\\
&b_c=\int_{\Omega_c}\psi^n u^*\,d\Omega.
\end{aligned} \tag{25}$$

Similar procedures are carried out for derivation of discrete equations for use with convection–diffusion or parabolic diffusion fundamental solutions.

5. Numerical algorithm

Since boundary conditions for vorticity transport equation are a priori unknown, velocity boundary conditions need to be supplied. For the calculation of boundary vorticity values, standard single domain BEM is used. Because of the solenoidality and compatibility constraints of the kinematics equation fully populated system matrix is needed. For a square discretized by $n \times n$ subdomains, we need approximately $4n \cdot n^2$ elements in the kinematics matrices. Thus, the memory requirements are quite high and are quickly increasing with mesh density. In order to reduce memory requirements, wavelet compression, as described by Ravnik et al. [19], can be used. Nevertheless this is still a memory bottleneck for the developed algorithm. All other parts of the numerical algorithm are discretized by subdomain BEM [13] governed by sparse rectangular non-symmetric system matrix which is then solved by LSQR type solver with diagonal preconditioning. These matrices scale with $\propto n^2$, thus with increasing mesh density their memory consumption becomes negligible in comparison with memory consumption of kinematics matrices. We can estimate then that memory consumption of the algorithm scales with n^3. The LSQR solver CPU requirements are comparable with other solvers that use diagonal preconditioning. Other types of preconditioning such as ILU for example usually further reduce number of iterations needed and CPU time but are unfortunately not applicable to the solver we use.

It has to be also noted that even though convection–diffusion fundamental solution is used, it does not match solution of Laplace equation for planar problems at its limit of $Re \to 0$. Consequentially the developed algorithm uses Laplace fundamental solution for stationary or its parabolic counterpart for non-stationary flows, when local Peclet number ($Pe_L = \sqrt{\overline{u_{cell}}^{2*CellArea}}/\nu_0$) in the subdomain falls below some user defined threshold value (T). $\overline{u_{cell}}$ is obtained by averaging values of each velocity component at cell corners.

Detailed algorithm is presented below:

- Calculation of integrals with Laplace fundamental solution kernel
- Begin time step
  - Choose local time derivative approximation
  - Start of global nonlinear loop
    - KINEMATICS: Calculate boundary vorticity values by solving kinematics equation (12) by single domain BEM
    - KINEMATICS: Calculate domain velocity values by solving kinematics equation (10) by subdomain BEM
    - Partitioning of velocity and viscosity fields over each subdomain in order to calculate integrals of convection–diffusion fundamental solution if needed
    - Vorticity KINETICS: Calculate domain vorticity values by solving vorticity transport equation (13) by subdomain BEM
    - Turbulence KINETICS: Calculation of turbulence models transport variables by solving equation(s) (21) if $Pe_L < T$ or (22) if $Pe_L \geq T$ by subdomain BEM and derivation of turbulence viscosity
    - Check convergence of nonlinear loop
  - End global nonlinear loop
- End time step and write results if needed

In the described algorithm, calculation of convection–diffusion fundamental solution integrals is made dependent on change of both velocity and viscosity fields by user defined value. Also, while testing the algorithm, it was established that those integrals need not to be calculated in every iteration of nonlinear loop. When calculating turbulence models, usually some kind of limiting procedure is advised, as described in Kuzmin et al. [20], Durbin [21].

6. Test cases

To validate the developed numerical algorithm, two two-dimensional test cases for turbulent flows were considered. The first test case was fully developed turbulent channel flow, and the second was turbulent flow over backward facing step. Results were then validated using available data. For all test cases threshold value for switching fundamental solutions was set to $T=2$.

6.1. Fully developed channel flow

At first, the developed algorithm was tested on a simple test case of two-dimensional turbulent channel flow. Three different turbulence models were used (see Table 1). Obtained results (in Figures denoted by BEM) were validated using available DNS

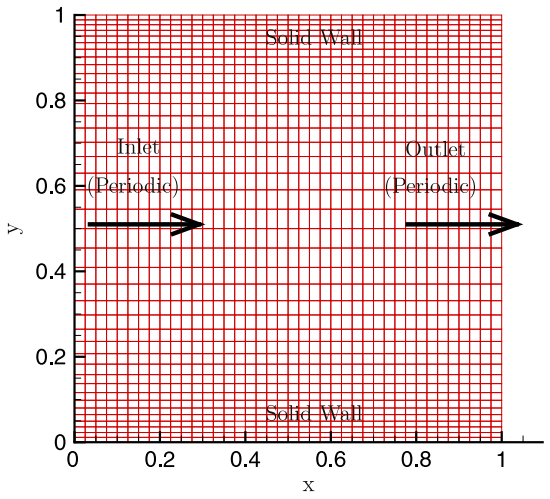

Fig. 1. Coarse mesh and boundary conditions for channel flow. Note that each subdomain includes nine mesh nodes.

data from Kim et al. [22] for lower turbulent Reynolds number $Re_\tau = 180$ and Mansour et al. [23], Moser et al. [24] for $Re_\tau = 395$. Two numerical meshes with different number of subdomains (cells) and slightly different geometry were used. Coarse mesh, shown in Fig. 1, was composed of 40×40 subdomains. It was mildly stretched in spanwise direction with 4:1 ratio of widest to narrowest subdomain. The domain had the geometrical form of unit square with edge length of $1H$. For a finer mesh a rectangular domain with 127×70 subdomains was used. In order to make sure that no influence of inlet boundary conditions to outlet was present, the domain was elongated in streamwise direction for a total length of $2H$. When taking this into consideration, the finer mesh had about 1.5 times more subdomains in streamwise direction and a little less than 2 times more subdomains in spanwise direction than a coarse mesh. The finer mesh also had a bit larger stretch ratio in spanwise direction of 6:1.

At both solid walls of the channel, no-slip boundary condition was prescribed as shown in Fig. 1, thus both velocity components were set to 0 and turbulence variable values were prescribed according to turbulence model specifications. At outlet boundary condition, zero normal derivative for all variables was prescribed, while function values were prescribed at the inlet section. When convergence criterion for vorticity field was achieved, periodic boundary conditions were applied on both ends of a channel for all variables.

6.1.1. $Re_\tau = 180$

For initial and inlet values of lower Reynolds number test case, previous results of laminar simulations were used. Since laminar solutions were obtained without using turbulence model, constant values were prescribed for turbulence variables at inlet section and inside solution domain. Simulations were then run for about 60 channel lengths until the velocity profile remained nearly constant. For both meshes results for velocity profiles written in wall coordinates ($U_x^+ = U_x/U_\tau$) are presented in Fig. 2 and the normalized turbulence kinetic energy profiles ($k^+ = k/U_\tau^2$) are presented in Fig. 3, where U_τ is the friction velocity. An additional comparison with Rahman and Siikonen [25] for turbulence kinetic energy is presented for Chien's [15] model. Since Spalart–Allmaras turbulence model [14] features only one transport equation for modified turbulence viscosity, no comparison could be made for turbulence kinetic energy. In all cases, good agreement with compared DNS data was obtained for velocity field even on coarse mesh. Use of a finer mesh yielded only a slight improvement in

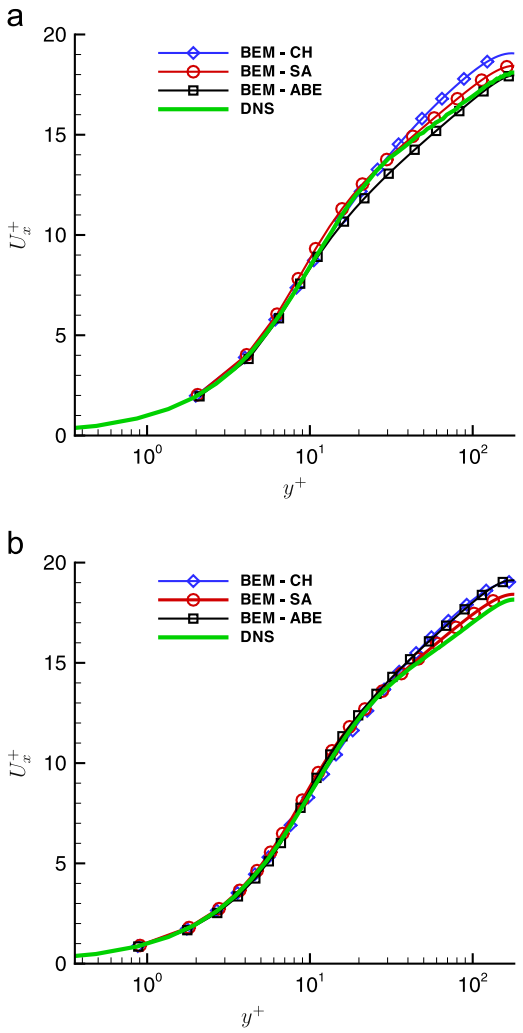

Fig. 2. Comparison of normalized velocity profiles of fully developed turbulent channel flow for BEM implementation of Chien, Spalart–Allmaras and Abe–Kondoh–Nagano turbulence models with DNS results [22]: $Re_\tau = 180$. (a) Coarse mesh and (b) Fine mesh.

results. The peak of turbulence kinetic energy was a bit underpredicted as expected (see Bredberg [26] or Rahman and Siikonen [27]). Comparison with FEM implementation of Chien's model by Rahman and Siikonen [25] shows practically identical results for the turbulence kinetic energy profile.

6.1.2. $Re_\tau = 395$

At the higher Reynolds number, results from $Re_\tau = 180$ were used as inlet and initial values for simulations. Results are presented in Figs. 4 and 5. On the coarse mesh we could not obtain converged results of Abe–Kondoh–Nagano model; results for the coarse mesh are therefore omitted. Again, results agree quite well with DNS data used for both meshes.

6.2. Flow over backward-facing step at $Re_h = 5000$

For our second test case flow over backward-facing step was chosen. Even though the geometry of this test case is fairly simple, calculation of the flow is quite a challenge for both numerics and turbulence models, since it features flow separation at fixed point, curved free shear layer and its bifurcation at reattachment point. Behind the step primary and secondary recirculation regions are formed. So-called flapping motions of primary recirculation region

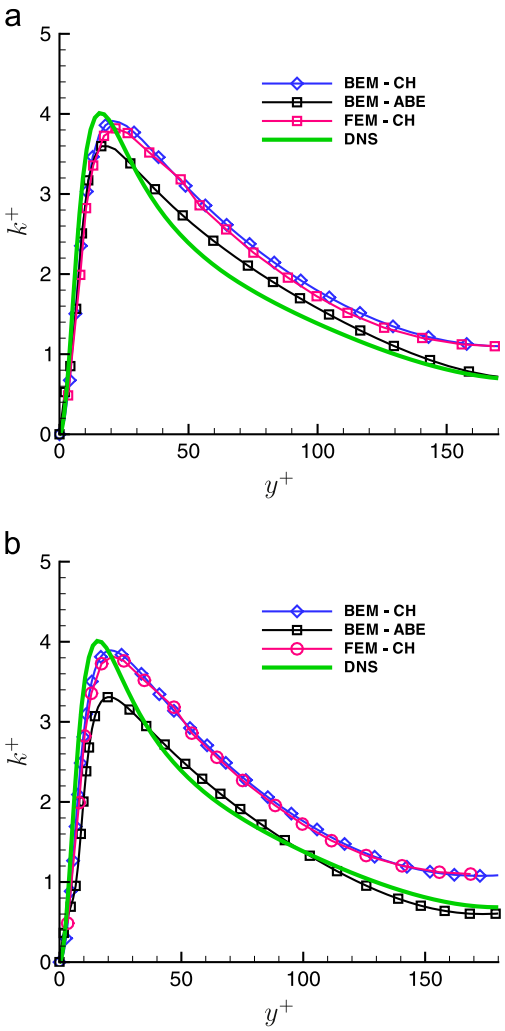

Fig. 3. Comparison of normalized turbulent kinetic energy profiles of fully developed turbulent channel flow for BEM implementation of Chien, Spalart–Allmaras and Abe–Kondoh–Nagano turbulence models with DNS results [22] and finite element implementation of Chiens model by Rahman and Siikonen [25]: $Re_\tau = 180$. (a) Coarse mesh and (b) Fine mesh.

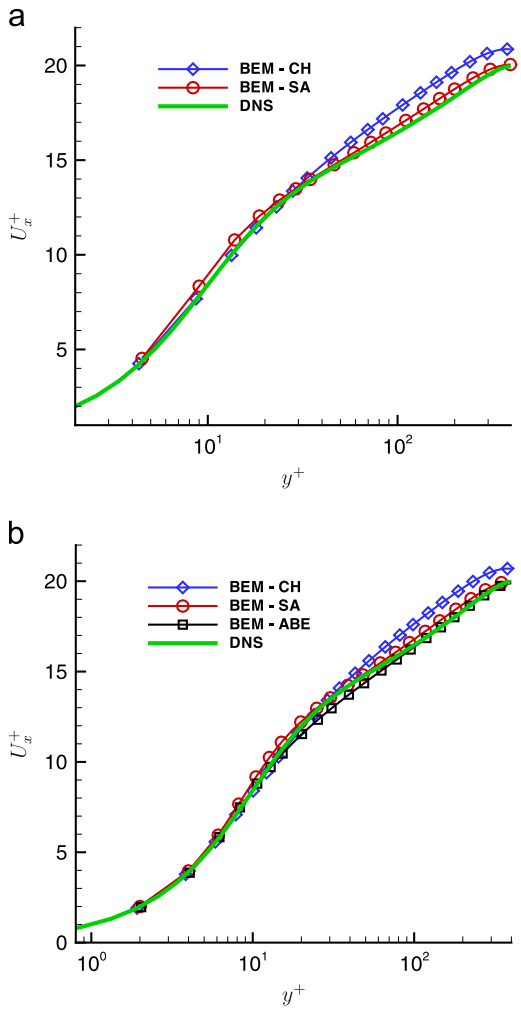

Fig. 4. Normalized velocity profiles section of fully developed turbulent channel flow for BEM implementation of Chien, Spalart–Allmaras and Abe–Kondoh–Nagano turbulence models with DNS results [23,24]: $Re_\tau = 395$. (a) Coarse mesh and (b) Fine mesh.

at low frequencies and roll-up and pairing of vortical structures at higher frequencies were observed by many authors experimentally [28–30] and numerically [31,32].

Geometry from Hanjalić and Jakirlić [33] was used for our test (Fig. 6) with top boundary condition as solid wall instead of symmetry. Calculation was performed on a mesh with 23 985 subdomains and 96 689 nodes. As characteristic dimensions step height (h) and velocity average at the inlet were chosen and used for the definition of Reynolds number (Re_h).

Three meshes of different density were used for the calculation of the flow with Chiens model. The coarsest mesh was composed of 16.8k subdomains (67.8k mesh nodes), mesh of middle density of 24.0k subdomains (96.7k mesh nodes) and the finest mesh was composed of 30.4k subdomains (122.4k mesh nodes). As can be seen in Fig. 7, the results on all meshes are similar, thus in further calculations the middle density mesh was used. Used mesh had, similar to Hanjalić and Jakirlić [33] and Ramšak and Škerget [11], first point upstream of step was at $y^+ \approx 5.6$ while at the outlet this value was at $y^+ \approx 4.5$. Because of y^+ dependence on friction velocity its values are even lower in recirculation regions.

For inlet boundary condition, results from previous channel flow simulations were used. Since transient simulations were performed in order to find converged steady state results after long time, convective boundary condition, as described by Orlanski [34], was used. On top and bottom walls no-slip boundary conditions were used.

It has to be noted that in literature two ways of calculation of expansion ratio are present. First uses full inlet channel height for its calculation as for example in Driver and Seegmiller [35], and other uses half of inlet channel height [33]. According to the first approach expansion ratio based on full inlet channel height for our geometry was $ER = 1.2$, and calculated by the second approach it was $ER = 1.33$.

Calculations were performed with Spalart–Allmaras and Chiens turbulence models. All simulations were started as stationary at Reynolds number 1000. Results were then used for initial conditions of simulation at intermediate $Re_h = 2000$. Non-dimensional time step $\Delta t = 0.1$ was chosen, normalized by $t = h/\overline{U}$, since steady flow simulation had trouble converging. Finally, simulations at $Re_h = 5000$, using results from $Re_h = 2000$ as initial values, were performed (Figs. 8 and 9).

It has been noted in Hanjalić and Jakirlić [33] that Durst and Schmidt [38] observed a monotonic increase in recirculation length by different authors, dependent on expansion ratio: $X_r \approx 5$ for expansion ratio of 1.1 to $X_r \approx 8.35$ for expansion ratio of 2. Also a steep increase in recirculation length was noticed by same authors from transient $Re_h = 4500$ to fully turbulent $Re_h \approx 100\,000$ Reynolds numbers. Based on these observations the expected recirculation length in our case should be around $x/h = 6$.

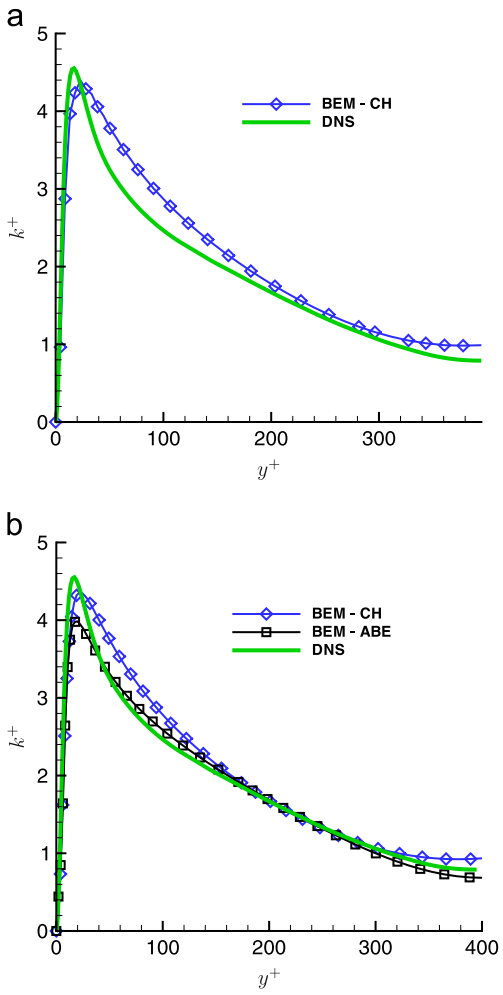

Fig. 5. Normalized turbulent kinetic energy profiles section of fully developed turbulent channel flow for BEM implementation of Chien, Spalart–Allmaras and Abe–Kondoh–Nagano turbulence models with DNS results [23,24]: $Re_\tau = 395$. (a) Coarse mesh and (b) Fine mesh.

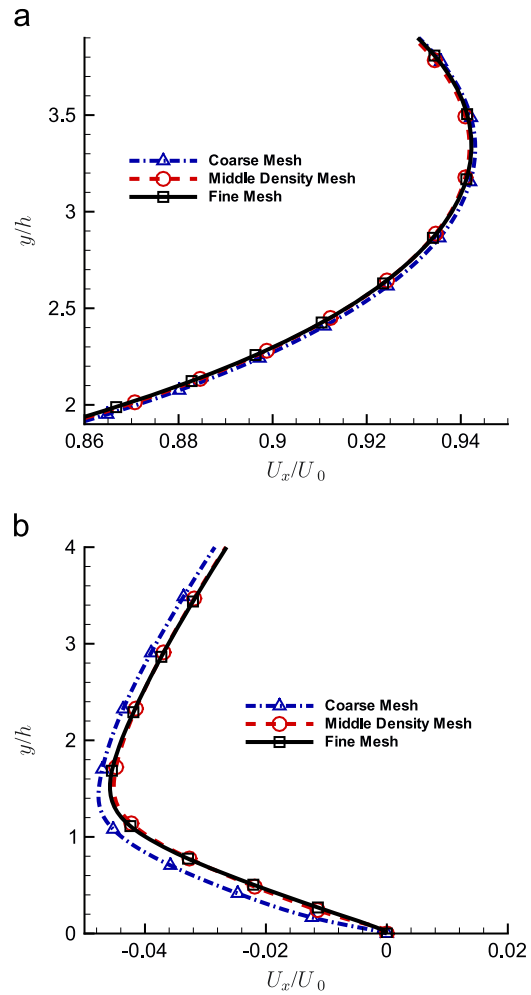

Fig. 7. Comparison of velocity profiles at $x/h = 6$ for different meshes: (a) streamwise velocity component and (b) spanwise velocity component, normalized by centerline velocity at inlet.

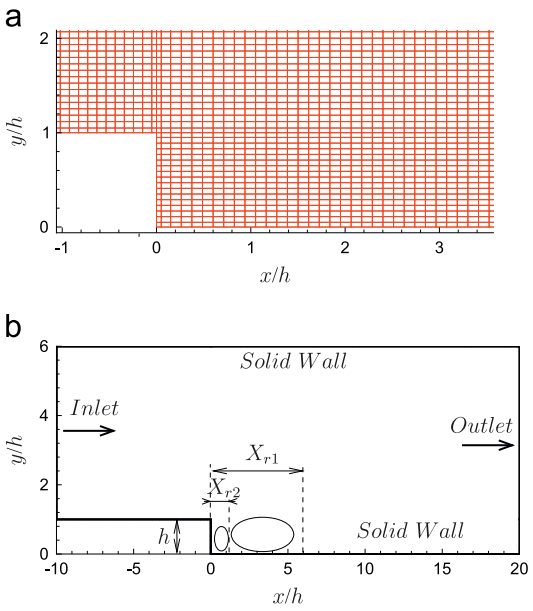

Fig. 6. Numerical mesh and boundary conditions used for calculation of backward-facing step flow. Note that each subdomain in the top figure includes nine mesh nodes. (a) Numerical mesh and (b) Boundary conditions.

It can be seen in Table 2 that primary and secondary recirculation length are comparable with results obtained by Ramšak and Škerget [11]. Primary recirculation length for both models falls well within the limits mentioned above.

Although unsteady simulations were performed, it was observed that after initial transient motion, simulations with both models come to an almost stationary result with only a slight periodic movement of primary recirculation region and a corresponding reattachment point. The conclusion is similar as by Fadai-Ghotbi et al. [31,32] that k–ε type models seem to be inappropriate for capturing unsteady effect on this type of flow. Also it is mentioned by Fadai-Ghotbi et al. [32] that unsteadiness could be attributed to numerical errors at corner of the step exciting natural mode of the shear layer.

Velocity profiles and friction coefficient at the bottom of the step are readily available from the experiment of Jović and Driver [36]. Albeit the experiment was performed at a different expansion ratio as our test case, Spazzini et al. [30] points out that a direct comparison should be possible by normalization of streamwise coordinate by the obtained primary reattachment position. Results for the friction coefficient are presented in Fig. 10. It can be seen that compared to the experiment, minimum values of friction coefficient are moved a bit upstream for both models used. Spalart–Allmaras model predicted minimum of friction coefficient quite well while non-physical local peak appeared right downstream of step wall. On the contrary, Chien's model performed

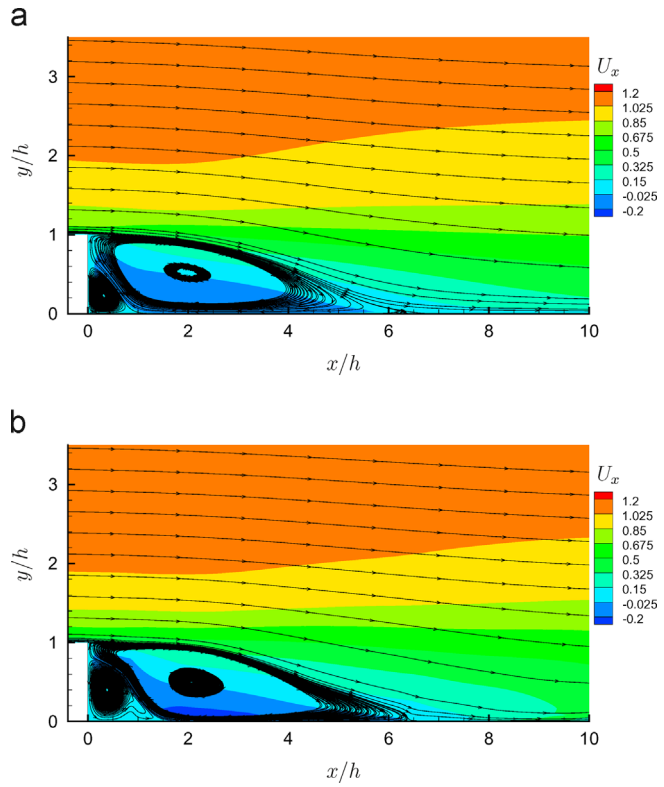

Fig. 8. Streamwise velocity contours and streamlines for backward-facing step flow at $Re_h = 5000$ for (a) Spalart–Allmaras and (b) Chien's models.

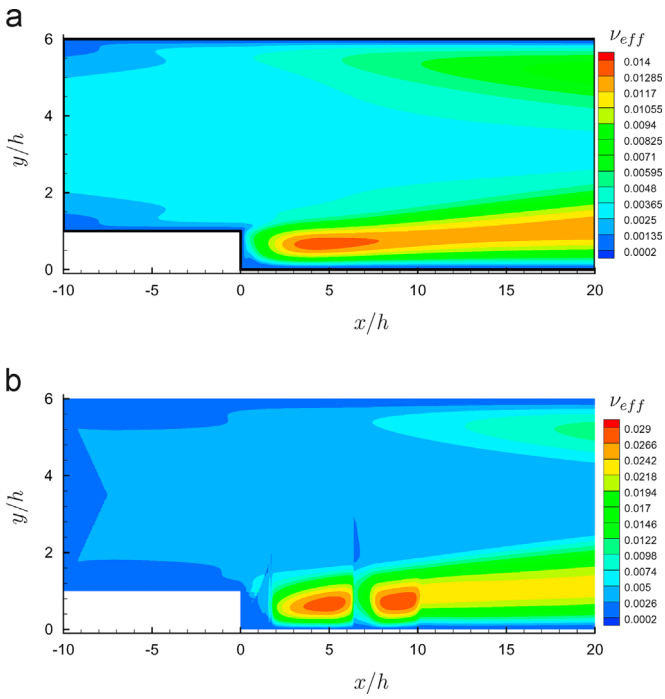

Fig. 9. Effective viscosity contours backward-facing step flow at $Re_h = 5000$ for (a) Spalart–Allmaras and (b) Chien's models.

better at the step wall, but predicted considerably lower global minimum of friction coefficient.

Lastly, we compare velocity profiles with the experiment performed by Jović and Driver [36] and direct numerical simulation of Le et al. [37]. Since expansion ratios (experiment, DNS and our test case) are quite high, similar profiles of velocity near the wall and larger discrepancies away from it were expected. Thus all velocity profiles were normalized with centerline velocity at inlet. Fig. 11a shows a comparison of streamwise velocity profiles and Fig. 11b spanwise velocity profiles at coordinate $x/h=6$. Good agreement was obtained for streamwise velocity component, while spanwise velocity profiles show similar discrepancies as can be seen in Hanjalić and Jakirlić [33] and DNS by Le et al. [37] in comparison with the experiment of Jović and Driver [36]. One has to note that albeit the relative error seems to be large, the absolute scale of the spanwise velocity profiles is about 20 times smaller than the scale of the streamwise velocity.

Table 2
Comparison of mean reattachment lengths for backstep flow.

Study	Expansion ratio	Primary X_{r1}	Secondary X_{r2}
Chien Ramšak [11]	1.33	5.81	1.19
FLB Ramšak [11]	1.33	4.52	0.30
exp Jović [36]	1.2	6.10	/
RSM Hanjalić [33]	1.2	6.38	1.55
DNS Le [37]	1.2	6.28	1.76
Spazzini [30]	1.31	5.39	1.8
BEM Chien Present	1.33	5.94	1.16
BEM SA Present	1.33	6.17	0.97

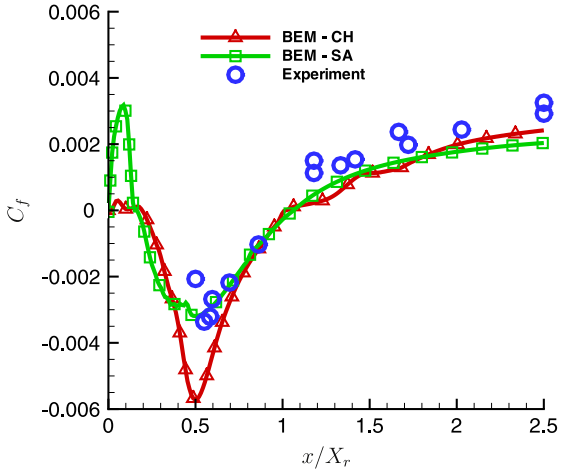

Fig. 10. Comparison of calculated skin friction coefficient for Spalart–Allmaras and Chien turbulence model with the experiment performed by Jović and Driver [36].

7. Conclusion

A boundary element based algorithm has been developed in order to solve turbulent flow using velocity–vorticity form of Navier–Stokes equations and low-Re turbulence models. The advantage of formulation used over the stream-function-vorticity formulation is the fact that the governing equations can be extended into three dimensions. Two different test cases were considered for testing purposes. Turbulent channel flow was calculated with three different turbulence models. Its results show good agreement with available DNS data of Kim et al. [22], Mansour et al. [23] and Moser et al. [24] even on the coarse mesh. Additional comparison was made with FEM implementation of Chien's model made by Rahman and Siikonen [25], which shows excellent agreement with their results. Computations with two different turbulence models were made for backward facing step flow. For improving convergence behavior unsteady simulations were used, but leading to an almost steady result. Reattachment lengths and behavior of friction coefficient were comparable with

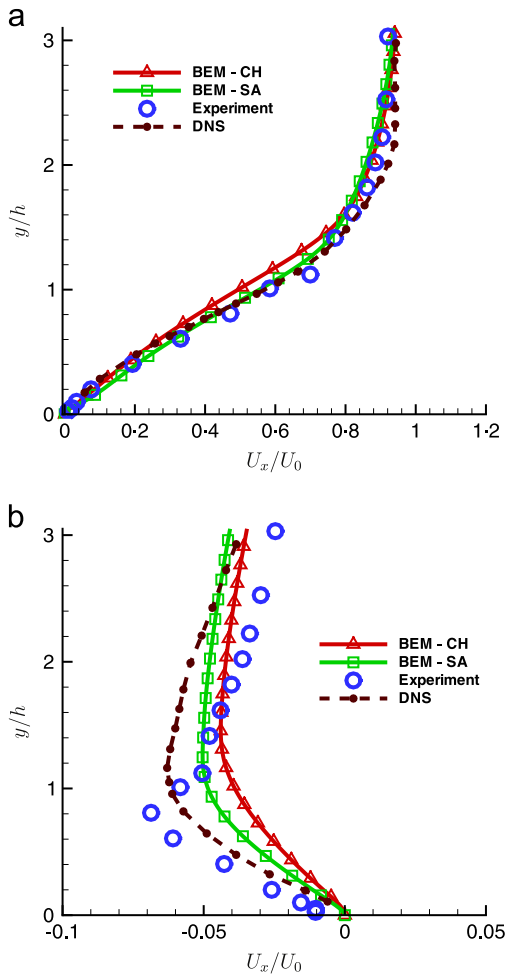

Fig. 11. Velocity profiles at $x/h=6$ for: (a) streamwise velocity component and (b) spanwise velocity component, normalized by centerline velocity at inlet. Compared with the experiment of Jović and Driver [36] and DNS by Le et al. [37]. (a) U_x profiles for $x/h=6$ and (b) U_y profiles for $x/h=6$

those available in literature. Overall, good agreement with available data was obtained for all test cases even on coarse meshes.

References

[1] Wrobel L, Brebbia C, Nardini D. The dual reciprocity boundary element formulation for transient heat conduction. In: Proceedings of the sixth international conference on finite elements in water resources, Lisbon, Portugal. 1986. p. 801–81.

[2] Wrobel L, Brebbia C. The dual reciprocity boundary element formulation for nonlinear diffusion problems. Comput Methods Appl Mech Eng 1987;65(2):147–64.

[3] Wrobel L, DeFigueiredo D. A dual reciprocity boundary element formulation for convection–diffusion problems with variable velocity fields. Eng Anal Bound Elem 1991;8(6):312–9.

[4] Taigbenu A. The Green element method. Int J Numer Methods Eng 1995;38(13):2241–63.

[5] Popov V, Power H. The DRM-MD integral equation method: an efficient approach for the numerical solution of domain dominant problems. Int J Numer Methods Eng 1999;44(3):327–53.

[6] Florez W, Power H, Chejne F. Multi-domain dual reciprocity BEM approach for the Navier–Stokes system of equations. Commun Numer Methods Eng 2000;16(10):671–81 dRBEM for NSand subdomains.

[7] Florez W, Power H, Chejne F. Numerical solution of thermal convection problems using the multidomain boundary element method. Numer Methods Partial Differential Equations 2002;18(4):469–89.

[8] Škerget P, Alujevič A. The solution of the Navier–Stokes equations in terms of vorticity–velocity variables by the boundary element method. Ges angew Math Mech Jahrestagung Goettingen West Germany Z Flugwissenschaften 1985;65:245.

[9] Škerget L, Hriberšek M, Žunič Z. Natural convection flows in complex cavities by BEM. Int J Numer Methods Heat Fluid Flow 2003;13(6):720–35.

[10] Škerget L, Ravnik J. BEM simulation of compressible fluid flow in an enclosure induced by thermoacoustic waves. Eng Anal Bound Elem 2009;33(4):561–71.

[11] Ramšak M, Škerget L. A multidomain boundary element method for two equation turbulence models. Eng Anal Bound Elem 2005;29(12):1086–103.

[12] Ravnik J, Škerget L, Hriberšek M. 2D velocity vorticity based LES for the solution of natural convection in a differentially heated enclosure by wavelet transform based BEM and FEM. Eng Anal Bound Elem 2006;30:671–86.

[13] Ramšak M, Škerget L. A subdomain boundary element method for high-Reynolds laminar flow using stream function-vorticity formulation. Int J Numer Methods Fluids 2004;46(8):815–47.

[14] Spalart P, Allmaras S. A one-equation turbulence model for aerodynamic flows. La recherche aérospatiale 1994;1(1):5–21.

[15] Chien K. Predictions of channel and boundary-layer flows with a low-Reynolds-number turbulence model. Am Inst Aeronautics Astronautics 1982;20:33–8.

[16] Abe K, Kondoh T, Nagano Y. A new turbulence model for predicting fluid flow and heat transfer in separating and reattaching flows—I. Flow field calculations. Int J Heat Mass Transfer 1994;37(1):139–51.

[17] Wrobel L, Aliabadi M. The boundary element methodapplications in thermo-fluids and acoustics. Wiley; 2002.

[18] Škerget L, Samec N. BEM for the two-dimensional plane compressible fluid dynamics. Eng Anal Bound Elem 2005;29(1):41–57.

[19] Ravnik J, Škerget L, Hriberšek M. The wavelet transform for BEM computational fluid dynamics. Eng Anal Bound Elem 2004;28(11):1303–14.

[20] Kuzmin D, Mierka O, Turek S. On the implementation of the κ–ε turbulence model in incompressible flow solvers based on a finite element discretisation. Int J Comput Sci Math 2007;1(2):193–206.

[21] Durbin P. On the k-3 stagnation point anomaly. Int J Heat Fluid Flow 1996;17(1):89–90.

[22] Kim J, Moin P, Moser R. Turbulence statistics in fully developed channel flow at low Reynolds number. J Fluid Mech 1987;177(1):133–66.

[23] Mansour N, Kim J, Moin P. Reynolds-stress and dissipation-rate budgets in a turbulent channel flow. J Fluid Mech 1988;194(1):15–44.

[24] Moser R, Kim J, Mansour N. Direct numerical simulation of turbulent channel flow up to $Re_\tau = 590$. Phys Fluids 1999;11:943.

[25] Rahman M, Siikonen T. Improved low-Reynolds-number k-epsilon-tilde model. AIAA J 2000;38(7):1298–300.

[26] Bredberg J. On two equation eddy-viscosity models. Chalmers University, Göteborg, Internal Report 2001;vol. 1 (8).

[27] Rahman M, Siikonen T. Near-wall turbulence modelling with enhanced dissipation. Int J Numer Methods Fluids 2003;42(9):979–97.

[28] Kiya M, Sasaki K. Structure of a turbulent separation bubble. J Fluid Mech 1983;137:83–113.

[29] Driver D, Seegmiller H, Marvin J. Time-dependent behavior of a reattaching shear layer. Am Inst Aeronaut Astronaut 1987;25:914–9.

[30] Spazzini P, Iuso G, Onorato M, Zurlo N, Di Cicca G. Unsteady behavior of back-facing step flow. Exp Fluids 2001;30(5):551–61.

[31] Fadai-Ghotbi A, Manceau R, Borée J. Revisiting URANS computations of the backward-facing step flow using second moment closures. influence of the numerics. Flow Turbulence Combust 2008;81(3):395–414.

[32] Fadai-Ghotbi A, Manceau R, Borée J. Revisiting URANS computations of the flow behind a backward-facing step using second moment closures. Comput Fluid Dyn 2009;2006:505–10.

[33] Hanjalić K, Jakirlić S. Contribution towards the second-moment closure modelling of separating turbulent flows. Comput Fluids 1998;27(2):137–56.

[34] Orlanski I. A simple boundary condition for unbounded hyperbolic flows. J Comput Phys 1976;21(3):251–69.

[35] Driver D, Seegmiller H. Features of a reattaching turbulent shear layer in divergent channel flow. Am Inst Aeronautics Astronautics 1985;23(2):163–71.

[36] Jović S, Driver D. Backward-facing step measurements at low Reynolds number, $Re_h = 5000$. NASA technical memorandum, vol. 108807; 1994. p. 1–24.

[37] Le H, Moin P, Kim J. Direct numerical simulation of turbulent flow over a backward-facing step. J Fluid Mech 1997;330(1):349–74.

[38] Durst F, Schmitt F. Experimental studies of high Reynolds number backward-facing step flow. In: 5th symposium on turbulent shear flows, vol. 1. 1985. p. 5.